The Astronomical Journal, 132:1023–1034, 2006 September

FAINT *U*-BAND DROPOUTS IN THE WFPC2 PARALLELS OF THE HUBBLE ULTRA DEEP FIELD

Yogesh Wadadekar,[1] Stefano Casertano,[1] and Duilia de Mello[2,3,4]

Received 2005 December 12; accepted 2006 May 9

ABSTRACT

We combine data from the extremely deep *Hubble Space Telescope U* (F300W) image, obtained using WFPC2 as part of the parallel observations of the Hubble Ultra Deep Field campaign, with *BVi* images from the Great Observatories Origins Deep Survey to identify a sample of Lyman break galaxies in the redshift range $2.0 \lesssim z \lesssim 3.5$. We use recent stellar population synthesis models with a wide variety of ages, metallicities, redshifts, and dust content, and a detailed representation of the H I cosmic opacity as a function of redshift to model the colors of galaxies in our combination of WFPC2 and ACS filters. Using these models, we derive improved color selection criteria that provide a clean selection of relatively unobscured star-forming galaxies in this redshift range. Our WFPC2 F300W image is the deepest image ever obtained at that wavelength. The 10 σ limiting magnitude measured over 0.2 arcsec^2 is 27.5 mag in the WFPC2 F300W image, about 0.5 mag deeper than the F300W image in the Hubble Deep Field (HDF)–North. This extra depth relative to the HDFs allows us to directly probe the luminosity function about 0.5 mag deeper than the depth accessible with the HDF data along an independent line of sight. Our sample of star-forming galaxies with $2.0 \lesssim z \lesssim 3.5$ includes 125 objects, the majority of which show clumpy morphologies. We measure a star formation rate density of 0.18 $M_\odot$ yr^{-1} Mpc^{-3}, marginally higher than the value measured for the HDFs.

Key words: cosmology: observations — galaxies: distances and redshifts — galaxies: evolution — galaxies: statistics — ultraviolet: galaxies

Online material: machine-readable table

1. INTRODUCTION

Great effort has been expended in the last decade to identify galaxies at high redshift. It is hoped that measurements of their luminosity and color evolution will place constraints on the star formation history of the universe and indirectly on the formation of large-scale structure. In this search for high-redshift galaxies, the Lyman continuum break technique has been successfully applied to detect galaxies at cosmological distances.

A characteristic feature in the UV spectrum of star-forming galaxies is the Lyman break, the sharp continuum discontinuity at 912 Å. The break is caused by absorption of UV photons with wavelength $\lambda < 912$ Å in the outer atmospheres of massive stars that produce such photons, in interstellar H I gas, and in intervening H I gas along the line of sight from the star-forming galaxy to the observer. At a redshift of $z \sim 3$, the Lyman break is redshifted longward of the *U* filter, so that galaxies have very low (or undetectable) flux in *U*. If the galaxy is star-forming, it has a high flux redward of the Lyman break, causing it to be bright in observed *B* and blue in colors such as $B - V$ or $V - I$. A color selection that identifies "*U* dropouts," i.e., galaxies that are blue in $B - V$ and very faint in *U*, would then preferentially select actively star-forming galaxies in the redshift range $2 \lesssim z \lesssim 3.5$. The same principle can be used to identify galaxies at higher redshifts by moving to a redder set of filters. For example, the *B* dropouts that have $z \sim 4.5$ can be effectively identified using *BVI* data.

Several research groups have identified and studied *U* dropout galaxies (see Giavalisco 2002 for a review). Ground-based studies, mostly carried out with the Keck telescope (e.g., Steidel et al. 2003 and references therein), have studied samples with deep imaging and spectroscopy over relatively large areas of sky (typically about 1000 arcmin^2), to a typical depth of $R_{AB} = 25.5$ largely set by the spectroscopic follow-up. These studies were complemented by samples identified using the Hubble Deep Fields (HDFs), two deep imaging surveys with the WFPC2 instrument aboard the *Hubble Space Telescope* (*HST*; Williams et al. 1996; Casertano et al. 2000, hereafter C00). The HDFs were used to identify and study *U*-dropout galaxies (Madau et al. 1996; Dickinson 1998; C00) to much deeper limiting magnitudes ($R_{AB} \sim 28.0$) but over a solid angle about 2 orders of magnitude smaller than the ground-based observations. The HDF samples were too faint for complete spectroscopic follow-up. The precision of *HST* photometry also ensures small random errors on color measurements. Another important advantage of the *HST* is its unprecedented angular resolution, which allows for a study of the main morphological characteristics of the *U*-dropout galaxies, even at high redshift. However, the small solid angle that the samples probe makes them susceptible to statistical fluctuations caused by small number statistics, galaxy clustering, and field-to-field variations. The amplitude of these fluctuations can be estimated by observing multiple fields separated by a large angular distance. Currently, the two HDFs provide the only two such fields on the sky.

The scientific success of the WFPC2 HDFs motivated an even deeper set of observations with the Wide Field Channel of the Advanced Camera for Surveys (ACS) installed on the *HST* in 2002 March. The Hubble Ultra Deep Field (HUDF; Beckwith et al. 2006) covered an area about twice that of each of the original deep fields and reached about 1.5 mag deeper in the *i* band.

The ACS Wide Field Channel has been optimized for visible and near-IR throughput and has very poor UV sensitivity. For this reason, the HUDF ACS observations were restricted to the

[1] Space Telescope Science Institute, 3700 San Martin Drive, Baltimore, MD 21218.
[2] Observational Cosmology Laboratory, Code 665, Goddard Space Flight Center, Greenbelt, MD 20771.
[3] Department of Physics, Catholic University of America, Washington, DC 20064.
[4] Department of Physics and Astronomy, Johns Hopkins University, Baltimore, MD 21218.

BViz (F435W, F606W, F775W, and F850LP) filters; *U*-band data were not obtained. The HUDF thus provides the deepest available sample of *B*-, *V*-, and *i*-dropout galaxies, but a study of *U* dropouts is not possible. However, in parallel with the HUDF ACS and NICMOS prime observations, data were gathered with all the other *HST* instruments in parallel mode. As part of these parallel observations, the WFPC2 instrument observed two fields using the F300W filter. Both these fields are considerably deeper than the HDF F300W observations. One of them overlaps with the coverage of the ACS Great Observatories Origins Deep Survey South (GOODS-S) field (Giavalisco et al. 2004) and thus has moderately deep *BViz* data from that survey. In this paper we combine data from the GOODS survey with the WFPC2 parallel observations of the HUDF to identify a new sample of *U*-band dropout galaxies. Our deeper *U*-band observations, relative to the HDFs, allow us to directly explore a region of the luminosity function of *U*-dropout galaxies that has never been directly probed before.

Throughout this paper, unless otherwise stated, we use the standard concordance cosmology with $\Omega_m = 0.3$, $\Omega_\Lambda = 0.7$, and $h_{100} = 0.7$. For magnitudes, we use the AB system of Oke & Gunn (1983). For convenience, we use the designations *U*, *B*, *V*, and *i* while referring to the WFPC2 F300W, ACS F435W, ACS F606W and ACS F775W filters, respectively.

This paper is organized as follows: In § 2 we describe our data and data processing procedures. In § 3 we describe the simulations we carried out to identify the appropriate color selection criteria for our dropout candidates and how we applied the criteria to identify our dropout sample. Section 4 describes the dropout morphology, and § 5 contains a discussion of dropout statistics.

2. THE DATA

In this paper we analyze the HUDF WFPC2 (F300W) parallels that overlap substantially over the GOODS-S area, i.e., the epoch1-orient 310/314 image (see Fig. 1 of de Mello et al. [2006] for a finding chart of this area relative to the GOODS-S field). The other WFPC2 parallel field (epoch 2-orient 40/44) overlaps with the Galaxy Evolution from Morphology and SEDs (Rix et al. 2004) survey area; because of the lack of *B*-band data this region cannot be studied in the same way and is not considered further in this paper. Each field includes several hundred exposures, with total exposure times of 323.1 and 278.9 ks, respectively. Because of small changes in the position angle of *HST* during each observing campaign, data at each epoch cover 6.52 arcmin^2, with 4.02 arcmin^2 at the full nominal depth (the three wide-field chips from all data sets overlapping), and the remaining 2.50 arcmin^2 for between 25% and 75% of the observing time. About 87% (5.67 arcmin^2) of the F300W image overlaps with the GOODS-S footprint, including almost the entire full-depth area (see Fig. 1).

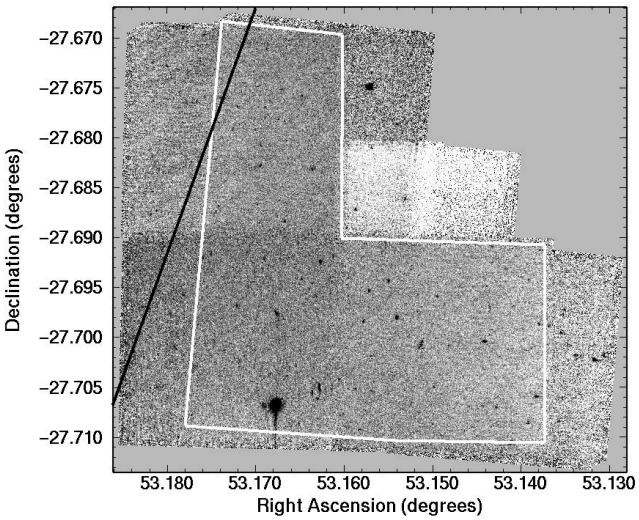

FIG. 1.—Final drizzled image in F300W obtained by combining 409 individual exposures. The white polygon encloses the area over which the wide-field chips of all data sets overlap to give a total exposure time of 323.1 ks; outside this area the effective exposure is between 25% and 75% of the full depth. Portions of the image above and to the left of the black line lie outside the GOODS area and are not useful for identifying *U*-dropout galaxies.

2.1. *Data Processing*

The data processing was carried out with the techniques developed for the WFPC2 Archival Pure Parallels Project (APPP; Wadadekar et al. 2006), based on the drizzle approach (Fruchter & Hook 2002). We constructed a drizzled image with a pixel scale of 0.″06 pixel^{-1}. The various procedures required to obtain a final combined image have been described in de Mello et al. (2006). For completeness, we repeat the data processing steps here.

For epoch 1, a total of 409 WFPC2 F300W parallel images, with exposure times ranging from 700 to 900 s, were obtained in parallel with the prime ACS observations. Each of the data sets was obtained at one of two orientations of the telescope: (1) 304 images obtained at orient 314 and (2) 105 images obtained at orient 310.

We downloaded all 409 data sets from the *HST* data archive along with the corresponding data-quality files and flat-field images. These data sets were all downloaded in a single request to the archive to ensure that the "on-the-fly reprocessing" procedure was identical for all the images. World Coordinate System (WCS) coordinates listed in the FITS header of WFPC2 images may be inaccurate by as much as an arcsecond, depending on the details of the *HST* guide star acquisition process. This inaccuracy can lead to relative offsets between images that contribute to the drizzle stack, as well as errors in the absolute positioning of the image on the sky.

The processing pipeline of the APPP registers images relative to each other using an automated procedure that employs matched source lists to compute the offsets. We modified this procedure by measuring the centroid positions of four predetermined stars in every image with respect to an arbitrarily chosen reference image. These stars are the only sources that are detectable in each individual exposure in our drizzle stack. The nominal WCS of each individual image in the drizzle stack was updated to reflect the improved relative alignment with respect to the reference image; after this WCS update the images were well registered with respect to the reference image. Given that we only had four stars to which to fit, we were unable to determine independent rotation corrections to a sufficiently high precision and therefore left unchanged the orientation of each individual image, correcting only for shifts in the position of the stars.

Our procedure also accounted for the shifts in the relative positions of the WFPC2 detector as a function of time using the model of Casertano & Wiggs (2001). Geometric distortion coefficients determined by Kozhurina-Platais et al. (2003) for the F300W filter were incorporated into the procedure. Cosmic-ray rejection was achieved using the procedure outlined by Fruchter & Hook (2002).

The processing was carried out in two stages. In the first stage images with near 100% overlap were grouped together in groups of 20 images each. Each group was processed separately. Such separate processing in groups was necessitated by memory

limitations on our computer. The drizzled image stack of 20 images was used to identify cosmic rays and store that information in a cosmic-ray flag image for each of the 20 images combined. This step was repeated for all the groups. In the second stage all 409 images were drizzled through to a final image using the cosmic-ray flag images to reject cosmic rays.

Offsets between our final drizzled image and the GOODS images were measured by matching sources in our image with the corresponding sources in the GOODS data, which were binned from their original scale of 0.″03 to 0.″06 pixel^{-1}. Once the offsets between the drizzled WFPC2 image and the GOODS images had been measured, all 409 images were drizzled through again, taking the offsets into account, so that the final image was accurately aligned with the binned GOODS images. This final image had an identical WCS to the binned GOODS images; this means that all sources had identical pixel coordinates in all filters and could thus be used for accurate dual-mode photometry, in which the image in one filter is first used for detection, and subsequent photometry is carried out in all filters using the segmentation map of the detection image. The residual scatter in source registration between the GOODS images and the WFPC2 image is random (20 mas rms) and is likely caused by the mismatch in the centroids of sources between the *U* and redder bands, which is probably due to the fact that the regions of peak UV emission in galaxies probed by the *U*-band image may not coincide with the peaks of light emission at redder wavelengths, leading to random offsets in centroid positions.

We weighted each drizzled data set by its inverse variance map during the drizzle process. This map was computed according to the prescription of C00. This computation of the variance takes into account contributions to the noise from the sky background (as modulated by the flat field), dark current, and read noise. Contributions to shot noise from sources are not included. Each weight map is combined with masks that exclude (i.e., set to zero weight) pixels that are flagged as bad in the data-quality files and is then used to weight the combination of images in the drizzle process. The drizzle process also produces a weight map as one of its outputs. The weight map is an accurate measure of the effective exposure (and therefore depth) that is reached at any particular location in the image after correctly accounting for missing data due to cosmic rays, hot pixels, etc., in each image that is being combined.

The WFPC2 CCDs have a small but significant charge transfer efficiency (CTE) problem that causes some signal to be lost when charge is transferred down the chip during readout (Heyer et al. 2004). The extent of the CTE problem is a function of target counts, background light, and epoch. Low-background images (such as those in the F300W filter) at recent epochs are more severely affected. Not only sources but also cosmic rays leave a significant CTE trail. We attempted to flag the CTE trails left by cosmic rays in the following manner: if a pixel was flagged as a cosmic ray, adjacent pixels in the direction of readout (along the *y*-axis of the chip) were also flagged as cosmic-ray affected. The number of pixels flagged depends on the position of the cosmic ray on the CCD, with more pixels flagged for higher row numbers. Only one pixel was flagged for rows 1 through 100, two pixels were flagged for rows 101 through 200, and so on. With this approach, we were able to eliminate most of the artifacts caused by cosmic rays in the final drizzled image.

The 10 σ limiting magnitude measured over 0.2 arcsec^2 is 27.5 mag over the $\sim$4 arcmin^2 field that has all 409 data sets overlapping, which is about 0.5 mag deeper than the F300W image in the Hubble Deep Field–North (HDF-N) and 0.7 mag deeper than that in the Hubble Deep Field–South (HDF-S). Somewhat lower depth is reached in the regions in which not all data sets overlap.

3. MODELING THE COLORS OF HIGH-REDSHIFT GALAXIES

3.1. *Evolutionary Population Synthesis Models*

In order to identify galaxies in the redshift range of interest, candidates first need to be identified in an appropriate color-color space of the available data. Such a selection function may be affected by many factors: the particular color criteria adopted, the intrinsic dispersion in the UV spectral properties of the star-forming galaxies (as influenced by differences in metallicity, stellar initial mass function [IMF], star formation history, and dust properties), the cosmic variance along different lines of sight, and the photometric measurement errors. This selection function can be estimated from models or measured directly by determining enough spectroscopic redshifts to measure it empirically. Empirical determination for space-based dropout samples is precluded for at least two reasons: (1) the faintness of the candidates makes spectroscopy difficult even with 10 m class telescopes, and (2) the clustering of Lyman break galaxies necessitates measurements over many independent sight lines to average over the effects of large-scale structure. The two deep fields provide the only currently available sight lines for *HST* data. We therefore need to use a model to obtain the color selection criteria that isolate high-redshift star-forming galaxies.

The colors of galaxies as a function of age, metallicity, stellar IMF, and star formation history can be effectively modeled using the evolutionary population synthesis technique (see Bruzual & Charlot 2003, hereafter BC03, and references therein). Assumptions about the time evolution of these parameters allow one to compute the age-dependent distribution of stars in the Hertzsprung-Russell diagram, from which the integrated spectrum for the entire galaxy can be obtained. The models exploit the property that stellar populations with an arbitrary star formation history can be thought of as the sum of a series of instantaneous starbursts (δ-functions), referred to as simple stellar populations (SSPs). The spectral energy distribution (SED) at time t of a stellar population characterized by a star formation rate (SFR) $\psi(t)$ and a metal-enrichment law $\zeta(t)$ can be written (following, e.g., Tinsley 1980)

$$F_\lambda(t) = \int_0^t \psi(t-t')\ S_\lambda[t', \zeta(t-t')]\ dt', \qquad (1)$$

where $S_\lambda[t', \zeta(t-t')]$ is the power radiated per unit wavelength per unit initial mass by an SSP of age t' and metallicity $\zeta(t-t')$. The above expression assumes that the IMF does not change with time. The largest source of uncertainty in the spectral synthesis technique arises from the relatively poorly understood advanced phases of stellar evolution, such as the supergiant and asymptotic giant branch (AGB) phases (BC03).

In this paper we use predictions from the BC03 model for the purpose of defining the color-selection criteria for *U*-dropout galaxies for the combination of ACS and WFPC2 filters specific to our data. We chose to use the BC03 model because it is a recent model that provides high-resolution spectra for our wavelength range of interest. The code implementing the model prescriptions, GALAXYEV, is publicly available from the authors, thus providing a means of making our simulations reproducible by other researchers.

We summarize here the main features of the BC03 model that are relevant for our purposes. The model predicts the spectral evolution of stellar populations of different metallicities and ages

between 1×10^5 and 2×10^{10} yr at a resolution of 3 Å FWHM over the whole wavelength range from 3200 to 9500 Å. These predictions are based on a new library of observed stellar spectra compiled by Le Borgne (2003) called STELIB. Predictions over a wider wavelength range but at lower resolution are also available. The Padova 1994 stellar evolution prescription and the BaSel 3.1 spectral calibrations are used. Two choices of IMF are available: the standard Salpeter (1955) IMF and the Chabrier (2003) IMF with lower and upper mass cutoffs of 0.1 and 100 $M_\odot$, respectively. Each model SSP is normalized to a total mass of 1 $M_\odot$ in stars. The spectra are computed at 221 unequally spaced SSP ages from 0 to 20 Gyr. Metallicity ranges from 0.005 to 2.5 $Z_\odot$.

The authors of BC03 have tested the predictions of their model against observed color-magnitude diagrams (CMDs) and integrated colors of star clusters. Overall, their model provides excellent fits to star clusters of different ages and metallicities in several photometric bands. They also compare the predictions of their model with observed galaxy spectra in the Early Data Release of the Sloan Digital Sky Survey (SDSS). Comparison of the strengths of various absorption features and Lick indices between the SDSS galaxies, the BC03 models, and other models shows a broad consistency between model and observations.

The spectrum of a star-forming galaxy, when observed over cosmological distances, is modified significantly by two effects: (1) intergalactic attenuation along the line of sight from the galaxy to the observer and (2) dust attenuation in the emitting galaxy. In order to obtain a realistic model of the observed galaxy spectrum, it is necessary to account for both these effects.

3.2. *Intergalactic Attenuation along the Line of Sight*

The model of Madau (1995) for the propagation of UV radiation through a clumpy universe is the standard work for determining intergalactic attenuation. This model for the H I opacity of the universe as a function of redshift includes scattering in resonant lines of the Lyman series (Lyα, Lyβ, Lyγ, and Lyδ) and Lyman continuum absorption. Recently, Meiksin (2006) has proposed a model based on more current estimates of the properties of the intergalactic medium. The results of numerical simulations were used to estimate the contributions to resonant scattering from the higher order Lyman transitions. Differences of 0.5–1 mag from the previous estimate of Madau are found. In this work we have chosen to use the standard work of Madau (1995) to enable us to make comparisons with previous work that have almost without exception used this H I attenuation model.

The amount of flux attenuation can be computed as a function of wavelength at each redshift of interest. We show in Figure 2 a plot of the transmitted power fraction as function of wavelength and redshift. The characteristic staircase profile is due to continuum blanketing by the Lyman series. At $z > 1.8$ the flux in the U-band is significantly lowered by the increased H I opacity. At higher redshifts, flux in progressively redder bands is affected.

3.3. *Attenuation by Dust in the Emitting Galaxy*

We use the simple but realistic prescription of Charlot & Fall (2000) to account for the attenuation of light by dust. In this prescription, the attenuation of starlight by dust is accounted for by inserting a factor $\exp[-\hat{\tau}_\lambda(t')]$ in the integrand on the right-hand side of equation (1), where $\hat{\tau}_\lambda(t')$ is the effective absorption curve describing the attenuation of photons emitted in all directions by stars of age t' in a galaxy. This is given by the simple formula

$$\hat{\tau}_\lambda(t') = \begin{cases} \hat{\tau}_V \left(\lambda/5500\ \text{Å}\right)^{-0.7}, & t' \leq 10^7\ \text{yr}, \\ \mu\hat{\tau}_V \left(\lambda/5500\ \text{Å}\right)^{-0.7}, & t' > 10^7\ \text{yr}, \end{cases} \quad (2)$$

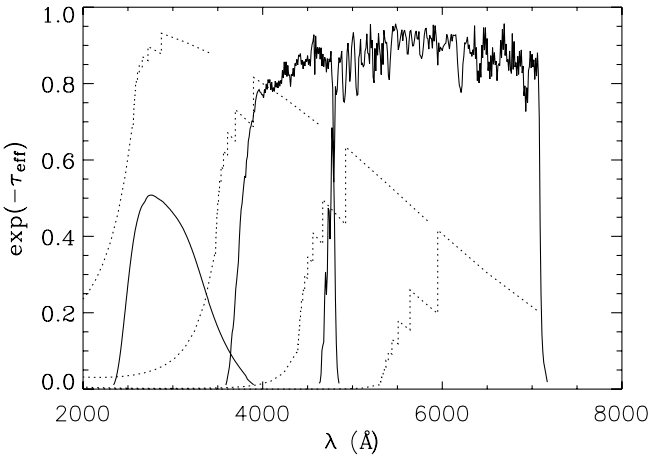

FIG. 2.—Mean transmission spectrum for a source at $z = 1.8$, 2.8, 3.8, and 4.8 (*left to right, dotted lines*) computed according to the model of Madau (1995). The characteristic staircase profile is due to continuum blanketing from the Lyman series. Also plotted are the response functions of our U, B, and V filters (*left to right, solid lines*).

where $\hat{\tau}_V$ is the total effective V-band optical depth seen by young stars. The characteristic age 10^7 yr corresponds to the typical lifetime of a giant molecular cloud. The adjustable parameter μ defines the fraction of the total dust-absorption optical depth of the galaxy contributed by the diffuse interstellar medium ($\mu \approx \frac{1}{3}$ on average, with substantial scatter).

3.4. *Our Simulations*

The main aim in our simulations is to exploit the combined effect of the intrinsic Lyman edge in galaxy spectra and the opacity of intergalactic H I gas to separate relatively unobscured star-forming galaxies from those that are older and/or dustier, in a color-color diagram of available broadband colors. Such a separation in color-color space is most effectively achieved by plotting the $U - B$ color against the $B - V$ or $B - I$ color. In practice the choice of $B - V$ or $B - I$ does not have a significant impact on the efficiency or completeness of the separation. Following C00, we chose the $B - V$ color as the redder color in our simulations.

We wish to compute colors for galaxies populating a grid of ages, metallicities, dust obscuration, and star formation histories at various redshifts. (See Table 1 for a summary of parameter grid values used in our simulations.) As a first step we need to study how the choice of IMF (Salpeter or Chabrier) affects the distribution of galaxies in the color-color space. The Chabrier IMF is identical to the Salpeter IMF for stars that are more massive than 1 $M_\odot$. For lower mass stars and substellar populations such as brown dwarfs the two IMFs are significantly different. However, the rest-frame UV emission from galaxies at high redshift that is probed by the colors used in our simulations receives a nearly negligible contribution from low-mass stars and brown dwarfs. Thus, for our simulations, choosing either IMF should produce nearly indistinguishable color-color plots. We verified this by comparing color-color plots for both IMFs in the relevant region of color-color space. For consistency with previous work we chose to use the standard Salpeter IMF in our models. There is no prior on which points on the grid are valid, except the obvious logical requirement that the galaxy should be younger than the age of the universe at that redshift. The grid thus samples the plausible range of galaxy properties without weighting the results with our knowledge of the actual distribution of galaxy

TABLE 1
PARAMETER GRID USED FOR COMPUTING SYNTHETIC SPECTRA

Parameter	Value
Ages (Gyr)	0.001, 0.0025, 0.005, 0.0076, 0.01, 0.025, 0.05, 0.1, 0.5, 1.0, 5.0, 10.0
Exponential star formation timescales (Gyr)	0.01, 0.1, 1.0, 5.0, 10.0, 30
Constant star formation durations (Gyr)	0.01
Metallicities ($Z_\odot$)	0.2, 0.4, 1.0
$\hat{\tau}_v$	0.01, 0.51, 1.01, 1.51, 2.01, 2.51
μ	0.02, 0.22, 0.42, 0.62, 0.82
Redshifts	0.2–7.0; step size: 0.2

color that can be derived from either observations or theoretical models.

We compute the SED of each galaxy by modeling it as a composite stellar population that formed either in a constant burst of star formation lasting 10^7 yr or in an exponentially decaying burst with timescales ranging from 10^6 to 3×10^{10} yr. The SEDs are computed at a range of ages (defined as the time since the onset of star formation) and with a range of metallicities. Note that all stars in a given galaxy have exactly the same metallicity in the BC03 model. Due to this, the changes in integrated colors due to metallicity gradients within a galaxy are not modeled. The SEDs are corrected for dust attenuation (§ 3.3), appropriately redshifted, and then flux-corrected for cosmic opacity along the line of sight (§ 3.2). Finally, the SEDs in the observer frame are folded through the filter response functions, and the broadband colors in the $U - B$ and $B - V$ filter are obtained.

3.5. *Colors of Relatively Unobscured Star-forming Galaxies at* $2.0 \lesssim z \lesssim 3.5$

We show in Figure 3 the color-color diagram that we obtained for our simulation of galaxies using the parameter grid described above. Colored symbols (*cyan through magenta*) identify galaxies within the desired redshift range $2 \lesssim z \lesssim 3.5$ that are both star-forming (age <0.1 Gyr) and relatively unobscured by dust [$\hat{\tau}_\lambda(t) < 2.0$]. Brown symbols identify old and/or attenuated galaxies in the same redshift range; such galaxies are typically much fainter in rest-frame UV (observed B) and are unlikely to constitute a large fraction of our sample. Black dots identify galaxies outside the target redshift range.

We find that relatively unobscured star-forming galaxies at $2 \lesssim z \lesssim 3.5$ are effectively selected in color-color space by the following color criteria: (1) $U - B > 1.0$, (2) $U - B > B - V + 1.3$, and (3) $B - V < 1.2$. The minimum "redness" threshold in $U - B$ color (Fig. 3, *horizontal line*) is motivated by the desire to exclude objects with $z < 2$. For a given metallicity and dust attenuation galaxies with $2 \lesssim z \lesssim 3.5$ become redder in $U - B$ at progressively higher redshifts while remaining relatively unaffected in their blue $B - V$ color. As the redshift approaches $z \lesssim 3.5$, the Lyα forest and eventually the Lyman limit begin to progressively intrude into the B band, causing the $B - V$ color to become redder. This begins to move galaxies rightward and out of the selection box. Increasing metallicity and dust obscuration both tend to make objects redder; the extent of the effect on each color is strongly dependent on the age of the population and the redshift.

By design, these selection criteria are aimed at identifying galaxies with strong UV flux. Therefore, our sample excludes galaxies with a low SFR or with strong reddening. The galaxies to the right of our $B - V$ cutoff in Figure 3 are relatively dusty [$\hat{\tau}_\lambda(t') \gtrsim 1.0$] and are forming stars at a relatively low rate. Such moderately reddened galaxies with modest star formation rates have been identified and studied spectroscopically at brighter magnitudes at somewhat lower redshift (Daddi et al. 2004; Reddy et al. 2005), but their luminosity function has not been probed directly to the faint levels we are investigating here. Similarly, recent ground-based studies (e.g., Le Fèvre et al. 2005) find a nonnegligible number of spectroscopically confirmed high-redshift galaxies below the selection box (bluer $U - B$ color). Again, these objects are significantly brighter ($I < 24$) than the objects that we aim to study in this work. Significantly expanding the selection box in either direction would include many more contaminating objects outside our target redshift range; therefore, we prefer to maintain a conservative selection criterion that keeps contamination low while including the majority

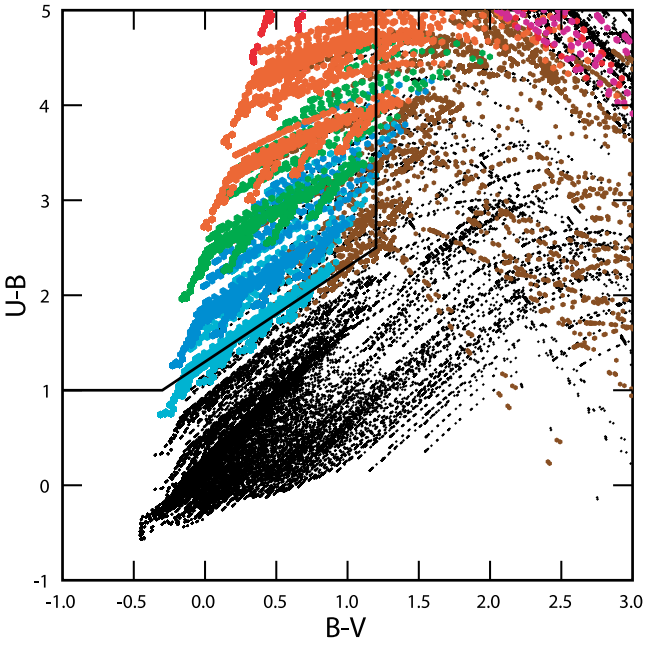

FIG. 3.—$U - B$ vs. $B - V$ for our simulated galaxies. A total of 264,600 synthetic spectra of galaxies representing a wide range of ages, star formation histories, metallicities, dust properties, and redshifts were folded through our combination of WFPC2 and ACS filters. Galaxies shown in colors other than black or brown represent young star-forming galaxies with relatively low levels of dust obscuration in the redshift range $2.0 < z < 3.5$. The colors cyan, blue, green, orange, red, and magenta show galaxies with progressively higher redshift in bins of 0.25 per color. Galaxies in the same redshift range that are old and/or severely dust attenuated are shown as brown dots. Black dots represent galaxies outside the redshift range. Our color selection criterion is shown by the polygon. Galaxies within the polygon are the *U*-band dropout candidate galaxies with $2.0 < z < 3.5$. The selection criteria are $U - B > 1.0$, $U - B > B - V + 1.3$, and $B - V < 1.2$.

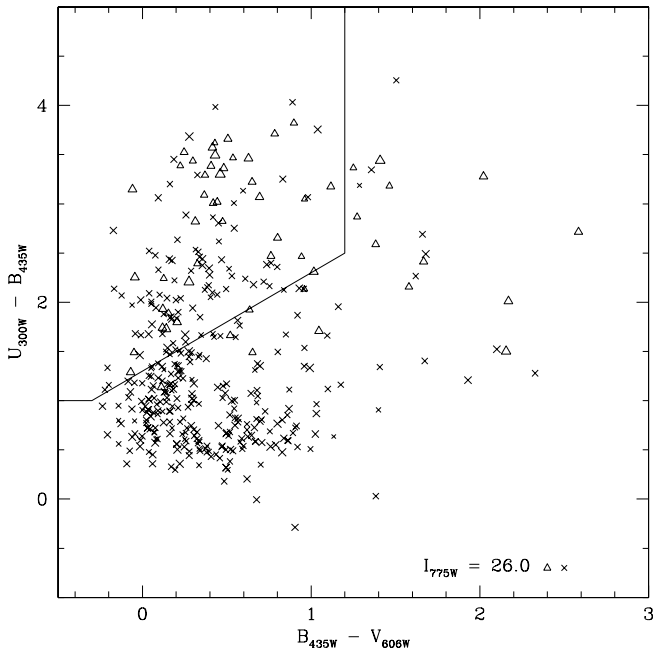

FIG. 4.—Color-color plot indicating the candidate *U*-band dropouts (enclosed by the polygon) in our data. Crosses indicate detections; triangles indicate nondetections in the *U*-band and are placed at the 1 σ lower limit of the $U - B$ color. The size of the symbols scales with magnitude in ACS F775W.

of strongly star-forming, relatively unobscured galaxies. This choice is consistent with that of other dropout studies, although our color limits are slightly different from C00 due to the updated stellar population models and to the fact that the ACS *B* (F435W) filter we use is shifted blueward of the WFPC2 *B* (F450W) filter.

3.6. *High-Redshift Galaxies in the HUDF Parallels: The Sample*

Having identified the color-selection criteria above, we are now in a position to identify *U*-dropout galaxies in our data. To obtain photometry for our images, we used SExtractor, version 2.3.2 (Bertin & Arnouts 1996), in dual-image mode. We used the GOODS/ACS *i*-band image for source detection and the WFPC2 *U*-band and GOODS/ACS *B*- and *V*-band images for photometry. The region of the GOODS data that fell outside the footprint of the *U*-band image was set to zero. Furthermore, 5.67 arcmin^2 (87%) of the 6.51 arcmin^2 footprint of our *U*-band image overlap with the GOODS coverage area (see Fig. 1).

The main advantage of dual-mode photometry is that there is no need to make a subjective decision to match corresponding sources detected in the various bands. Setting up such a correspondence is particularly difficult in situations in which a single object in one filter gets detected as multiple objects in another filter if there are multiple peaks in the light distribution. Such a situation is common in the *U* band, which selectively probes the regions of ongoing star formation within a galaxy. Detection was carried out with a `DETECT_MINAREA` of 12 pixels and a `DETECT_THRESH` of 1.5. The detections were filtered with a Gaussian kernel with FWHM 2.5 pixels and cleaned with `CLEAN_PARAM` = 1.0. Object deblending was carried out with `DEBLEND_MINCONT` = 0.03

The sample is first truncated at magnitude limits sufficiently bright that Lyman breaks of the expected amplitude could be measured reliably. For our data, this corresponds to $B < 27.3$. We find that all objects that are brighter than this limit in the *B* band are also detected in the *i*-band image. We show in Figure 4 the color-color plot highlighting the candidate *U*-band dropouts. Objects with measured magnitudes in all three bands are indicated by crosses. Objects with measured *U*-band flux (as indicated by the SExtractor `MAG_AUTO` magnitude) fainter than the 1 σ limit computed from the inverse variance map at that location are considered undetected and are marked by a triangle at the $U - B$ color corresponding to the 1 σ magnitude limit. The 1 σ limit depends on the size of the object. In addition, as the exposure time is not uniform across the image, it also varies with position. The size of each symbol is proportional to the *i*-band magnitude of the object.

The polygonal selection region that identifies *U*-band dropouts, as defined in § 3.5, contains 136 objects, each of which has been visually inspected. Five objects, all relatively bright ($i < 22$), appear to be stars; six more objects are otherwise spurious, due to either instrumental artifacts (diffraction spikes or image edges) or resolved segments of nearby bright galaxies. These 11 objects are not plotted in Figure 4 and have been excluded from the subsequent analysis. The remaining clean sample of *U* dropouts consists of 125 objects; their coordinates and magnitudes are listed in Table 2.

4. DROPOUT MORPHOLOGY

At redshifts $z \sim 3$ the drizzled ACS images with a resampled pixel scale of 0.″03 pixel^{-1} probe regions as small as 0.23 kpc pixel^{-1} for our chosen cosmology. The fine resolution provides sufficient resolution elements to enable at least a crude study of their morphology. The drizzled GOODS ACS images have the advantage of a pixel scale that is a factor of 2 finer than the drizzled HDF images. However, the depth reached by the GOODS survey is about a magnitude shallower than the corresponding HDF data. Morphological details can thus be studied with better resolution but poorer signal-to-noise ratio relative to the HDF images.

We have visually inspected the entire sample of *U* dropouts in the original GOODS ACS *z*-band images and classified their morphology using an empirical classification scheme. Objects that appear to be single and compact are classified as clumps (class 1), double or multiple clumps (chains) are class 2, and clumps with tails, i.e., tadpoles, are class 3. Objects that are not compact but extended and fuzzy are class 4, and fuzzy extended objects with a more organized disklike structure are class 5. Figure 5 illustrates typical objects of each class. We list in Table 3 the relative fraction of each class. For our sample, the fraction of single clumps is similar to the fraction of fuzzy objects (~35%); however, if double clumps and tadpoles are included in the clump class 1, this fraction increases to ~50%. The morphological classification for each object and short remarks on its appearance are listed in Table 2. We also show in Figure 6 *BVi* color composites of 16 typical bright dropouts in our sample.

Since the original deep fields, it has been known that compact/clump objects dominate at faint magnitudes (Abraham et al. 1996; van den Bergh 2002). Recently, this result has been confirmed by morphological studies of the HUDF, in which most of the galaxies are found to be clumps (Elmegreen et al. 2005; Elmegreen & Elmegreen 2005). An important question is whether such clumpy structures are signatures of merging/accretion or are merely a band-shifting effect. The latter is probably not the case, since these clumps have no counterparts in the local universe (Elmegreen et al. 2005; Elmegreen & Elmegreen 2005; Windhorst et al. 2002). Moreover, as shown in Papovich et al. (2005) for galaxies at $1.9 < z < 3$, there is very little morphological transformation between

TABLE 2

U-BAND DROPOUTS

$\alpha_{J2000.0}$ (deg)	$\delta_{J2000.0}$ (deg)	U	B	V	i	Class	Remarks
53.137048	−27.712829	27.54	24.48	24.39	24.30	3	Tadpole
53.145949	−27.710505	27.08	25.13	25.05	24.97	4	Fuzzy
53.164155	−27.709900	29.11	25.86	25.03	24.74	5	Faint clumpy disk
53.130524	−27.709571	>28.18	25.36	25.05	24.40	5	Disk/clumpy or double clump
53.157444	−27.709015	29.17	25.13	24.24	23.99	2	Double clump
53.171374	−27.709446	28.82	26.44	26.09	25.93	1	Faint clump
53.156550	−27.708817	28.48	26.96	26.77	26.80	1	Faint clump
53.166266	−27.708565	28.08	26.23	26.06	26.08	1	Clump
53.155762	−27.708305	29.53	26.47	25.48	25.12	5	Clumps in disk
53.166611	−27.708280	28.57	26.53	26.38	25.89	4	Faint fuzzy
53.160557	−27.707669	27.35	25.68	25.33	24.77	2	Multiple clump (maybe on faint disk)
53.130624	−27.707912	>28.86	27.12	27.00	26.39	5	Faint clumpy disk/tail?
53.150609	−27.707880	27.90	25.67	25.48	25.47	4	Faint fuzzy
53.153684	−27.707186	27.34	25.25	24.83	24.63	4	Fuzzy/clump
53.150374	−27.706826	27.59	25.05	24.74	24.46	5	Faint clumpy disk
53.131003	−27.706498	26.94	25.27	25.23	24.65	1	Clump
53.143096	−27.705956	29.69	26.80	26.54	26.50	5	Faint clumpy disk
53.175579	−27.705782	27.35	25.20	24.82	24.62	2	Double clump; merging
53.130086	−27.705758	>28.89	26.69	26.41	26.31	4	Faint fuzzy
53.173130	−27.705631	28.91	26.77	26.28	26.07	4	Faint fuzzy
53.182801	−27.705272	27.09	24.57	24.53	24.55	1	Clump edge-on
53.135928	−27.705299	29.00	26.97	26.98	26.86	4	Faint fuzzy
53.181991	−27.705029	28.49	26.90	26.72	26.76	4	Fuzzy
53.150622	−27.704625	27.38	25.40	25.35	25.32	1	Clump off-center
53.174787	−27.704499	>30.11	26.65	26.02	26.09	4	Faint fuzzy close to spiral
53.148378	−27.704298	29.81	26.06	25.02	24.72	1	Clump (spheroid)
53.165698	−27.703950	>29.90	26.83	26.14	25.94	4	Very faint fuzzy
53.131169	−27.703968	27.86	25.85	25.80	25.74	1	Clump/edge-on
53.130501	−27.703690	28.37	26.23	26.40	25.77	5	Fuzzy disk
53.175991	−27.703135	>30.43	26.91	26.66	26.67	1	Faint clump
53.149082	−27.702952	28.75	26.02	26.20	26.24	1	Clump/edge-on
53.141871	−27.702771	28.44	27.11	27.31	27.01	4	Fuzzy
53.137756	−27.701292	>29.65	26.26	25.85	25.71	1	Faint clump off-center on fuzzy tail (companions)
53.129540	−27.701279	>28.96	27.23	27.09	26.74	1	Clump next to peculiar shape disk (multiple clump?)
53.141437	−27.701159	28.99	27.11	26.99	26.53	6	Very faint
53.138861	−27.701083	27.26	25.67	25.41	25.01	1	Clump
53.178458	−27.701173	28.77	27.23	27.08	26.33	5	Faint disk edge-on
53.138012	−27.701123	>29.91	26.55	26.07	25.91	1	Clump/close to other faint clumps
53.161515	−27.684979	28.00	26.06	25.77	25.59	1	Clump/tail close to fuzzy
53.161355	−27.685116	27.33	25.65	25.69	25.86	4	Fuzzy close to clump/tail
53.145630	−27.685261	>27.88	25.41	24.65	24.44	1	Clump (spheroid)?
53.165419	−27.685627	28.87	26.59	26.19	26.07	4	Fuzzy
53.142972	−27.685698	26.93	25.47	25.49	25.27	5	Faint disk edge-on
53.140820	−27.685880	>28.09	26.60	26.65	26.47	5	Fuzzy/disky
53.143404	−27.686231	>28.72	26.83	26.68	26.53	2	Double clump
53.147907	−27.687704	27.95	26.27	26.15	26.26	2	Big chain
53.146281	−27.688363	>28.47	26.68	26.47	26.33	4	Fuzzy close to fuzzy objects
53.147855	−27.688591	>28.37	26.44	26.32	26.21	2	Chain
53.161346	−27.688836	28.73	26.30	25.83	25.55	4	Fuzzy/edge-on
53.154624	−27.689418	>30.31	27.16	27.22	27.30	1	Faint clump
53.143049	−27.689724	>28.62	26.38	26.25	26.21	4	Fuzzy
53.169292	−27.689970	28.38	26.04	25.53	25.40	1	Clump
53.145409	−27.690203	27.94	25.89	25.48	25.40	2	Clump
53.145325	−27.690252	29.20	26.06	25.47	25.37	2	Clump
53.157550	−27.690485	26.89	24.57	24.28	24.17	5	Off-center clump on disk?
53.168747	−27.690490	>29.85	26.19	25.68	25.52	2	Double clump
53.153418	−27.691316	>30.09	26.79	26.42	26.13	4	Several fuzzy
53.142828	−27.691609	29.83	27.19	26.98	27.02	4	Several fuzzy
53.177363	−27.691677	>29.75	26.70	25.74	25.36	1	Clump edge-on
53.143354	−27.691769	>30.36	26.87	26.44	26.38	1	Clump
53.128688	−27.692143	28.90	26.83	26.96	26.65	5	Faint clumpy disk?
53.132644	−27.692107	>29.36	27.10	27.15	27.12	1	Faint clump
53.172935	−27.692512	>30.17	26.95	26.30	26.08	2	Faint double
53.153738	−27.692797	29.14	26.74	25.98	25.79	1	Faint clump edge-on (tadpole?)
53.147447	−27.693511	>29.98	26.80	25.69	25.38	2	Double clump

TABLE 2—*Continued*

$\alpha_{J2000.0}$ (deg)	$\delta_{J2000.0}$ (deg)	U	B	V	i	Class	Remarks
53.144209	−27.693704	29.86	26.57	26.24	26.17	1	Faint clump
53.161386	−27.694332	27.15	24.64	24.31	24.09	2	Chain/three clumps
53.134128	−27.694236	29.45	27.29	26.53	26.14	4	Fuzzy
53.168314	−27.694244	28.74	26.89	26.55	26.03	4	Fuzzy
53.174811	−27.694860	29.50	25.51	25.08	24.84	1	Clump (faint tail?)
53.159129	−27.695401	>30.07	26.50	26.09	25.82	4	Fuzzy
53.141777	−27.695409	>30.19	26.76	26.46	26.39	4	Faint fuzzy edge-on
53.176046	−27.695456	>30.24	27.22	26.78	26.56	1	Faint clump
53.161879	−27.695566	>29.71	25.89	24.99	24.76	3	Tadpole
53.156940	−27.695521	30.05	27.19	26.77	26.76	1	Faint clump close to face-on spiral
53.134625	−27.695697	>29.11	26.02	25.65	25.68	4	Fuzzy
53.130320	−27.695894	>28.80	25.50	25.04	24.81	3	Tadpole
53.166073	−27.695896	29.41	25.96	25.77	25.76	1	Fuzzy
53.159225	−27.695951	29.04	26.95	26.91	27.21	1	Faint clump
53.132461	−27.696248	>29.16	26.70	25.76	25.55	3	Double clump
53.143279	−27.696576	29.80	26.99	26.54	26.51	1	Fuzzy close to face-on spiral
53.138781	−27.696842	29.28	26.90	26.16	25.60	1	Fuzzy extended
53.133936	−27.696977	28.51	26.03	25.96	25.55	1	Fuzzy extended
53.151536	−27.697612	27.68	25.60	25.16	24.87	3	Tadpole
53.136554	−27.697853	28.24	27.08	27.28	27.36	4	Fuzzy
53.145437	−27.697987	26.50	24.67	24.46	24.43	3	Tadpole?
53.173859	−27.698226	>29.78	26.40	26.17	25.65	4	Faint fuzzy
53.152117	−27.698154	28.77	26.31	25.97	25.86	3	Tadpole?
53.174661	−27.698140	28.40	26.58	26.41	26.39	4	Fuzzy
53.136690	−27.698376	28.87	27.09	27.04	27.04	4	Fuzzy
53.160346	−27.698494	29.34	26.98	26.18	26.05	4	Fuzzy
53.133898	−27.698699	27.34	25.87	25.71	25.40	4	Fuzzy
53.149444	−27.698816	29.62	27.29	27.20	26.96	1	Faint clump
53.182675	−27.698849	29.16	26.41	25.86	25.59	1	Clump
53.162550	−27.698872	29.10	26.68	26.50	26.72	4	Fuzzy, fuzzy companions
53.162513	−27.699074	29.20	27.03	26.64	26.49	4	Fuzzy, fuzzy companions
53.178276	−27.699784	29.03	26.95	26.85	26.81	4	Fuzzy with fuzzy companion
53.172033	−27.684078	28.57	26.31	25.78	25.47	4	Fuzzy
53.180185	−27.699950	27.80	25.90	25.69	25.56	2	Faint double clump/tadpole?
53.137583	−27.700109	29.01	26.01	25.46	25.09	1	Clump (spheroid) or faint star?
53.169918	−27.683871	28.82	26.61	25.89	25.60	4	Fuzzy
53.138746	−27.700467	>29.76	26.05	25.26	25.00	2	Four clumps
53.172890	−27.683628	>30.20	27.19	26.77	26.32	1	Faint clump
53.173737	−27.700799	29.27	26.83	26.67	26.91	4	Fuzzy
53.172186	−27.683993	>30.07	27.25	26.77	26.30	4	Faint fuzzy, close to clump
53.143580	−27.683502	>28.12	25.72	25.40	25.24	4	Fuzzy
53.169913	−27.669889	>30.22	26.60	26.17	25.77	1	Clump
53.161684	−27.682908	28.35	26.69	26.70	26.96	1	Clump
53.163174	−27.669346	27.54	25.20	24.80	24.67	5	Clumpy disk
53.161053	−27.672755	29.26	27.02	26.41	26.23	1	Clump
53.140722	−27.682237	>28.08	26.79	26.86	26.53	4	Faint fuzzy
53.166505	−27.672539	29.80	27.19	26.73	26.54	4	Fuzzy
53.160749	−27.671728	27.15	25.48	25.23	25.08	4	Fuzzy
53.164593	−27.674991	>29.94	26.48	25.94	25.89	4	Fuzzy
53.158301	−27.680860	>29.15	26.50	25.70	25.33	4	Fuzzy
53.169616	−27.672793	28.89	26.71	26.06	25.62	3	Tadpole
53.158060	−27.673707	28.22	25.78	25.42	25.19	2	Three clumps, chain
53.161286	−27.679136	28.91	26.94	27.00	27.11	1	Clump
53.158157	−27.673807	27.09	25.05	24.83	24.69	2	Double clump
53.162497	−27.671140	28.45	26.32	25.95	25.85	5	Fuzzy edge-on disk
53.165407	−27.674053	30.12	26.92	26.76	26.57	4	Faint fuzzy
53.169762	−27.674803	28.17	27.06	27.28	27.27	4	Fuzzy
53.152429	−27.677562	27.89	26.39	26.25	26.16	4	Fuzzy
53.156011	−27.676234	28.80	25.11	24.83	24.80	3	Tadpole? or peculiar disk
53.157810	−27.676274	28.84	26.82	26.62	26.43	4	Fuzzy

NOTE.—Table 2 is also available in machine-readable form in the electronic edition of the *Astronomical Journal*.

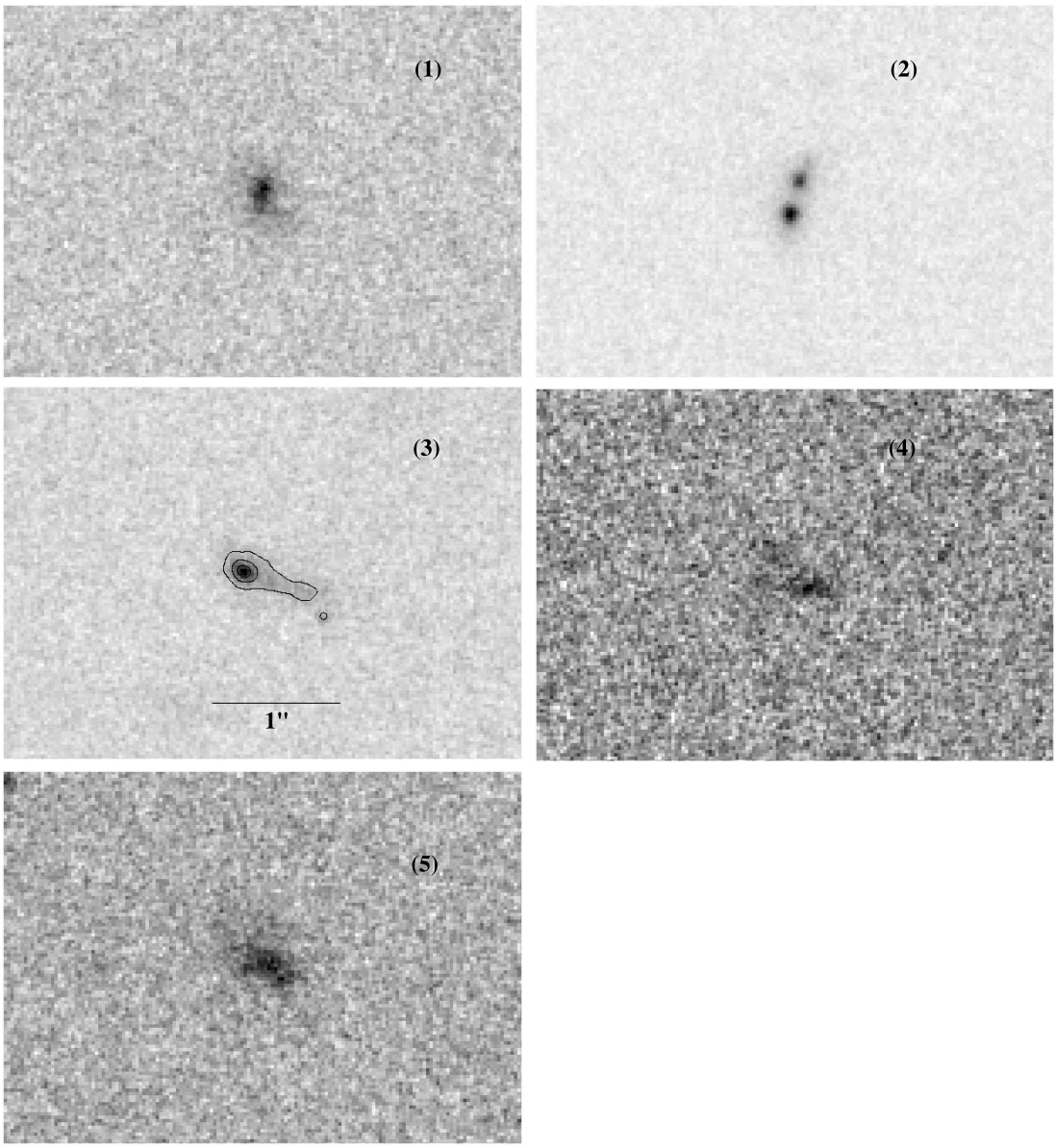

FIG. 5.—Representative dropout in each of the five classes into which we classify objects. The classes are (1) clumps, (2) double or multiple clumps, (3) clumps with tails, i.e., tadpoles, (4) objects that are not compact but extended and fuzzy, and (5) fuzzy extended objects but with a more organized disklike structure.

wavelengths using the WFPC2 F606W image and NICMOS F160W, which spans a long wavelength baseline (rest-frame far-UV to the rest-frame *B* band).

We have also checked whether the morphological counterparts of *U* dropouts are seen in the lower redshift ($z < 2$) sample (de Mello et al. 2006) for which we have photometric redshifts from GOODS (Dahlen et al. 2005). We found that *U*-dropout objects show morphological similarities to ones classified in de Mello et al. (2006) as starbursts,[5] which are classified as "compact, peculiar or low surface brightness (LSB)." The objects classified as "compacts" are similar to class 1. Objects in classes 2 and 3 would fit into the de Mello et al. "peculiar" class, and objects classified as class 4 (fuzzy) correspond to the LSB class. However, as expected, the *U*-dropout sample lacks the classical Hubble types, such as the elliptical/spheroid galaxies and disks that are seen at lower redshifts ($z < 0.8$). The fraction of LSBs and compact+peculiar objects in the sample of de Mello et al. (2006) that are at $0.8 < z < 1.2$ is 27% and 52%, respectively. Interestingly, the corresponding fractions of *U* dropouts are very similar, 38% and 51% (extended fuzzy

TABLE 3

MORPHOLOGICAL CLASSIFICATION OF *U*-BAND DROPOUTS MADE USING VISUAL EXAMINATION OF GOODS ACS *z*-BAND IMAGES

Morphological Class	Fraction (%)
Single clump	31
Double or multiple clump	13
Clump with tail	7
Extended and fuzzy	38
Fuzzy, extended with disklike structure	11

NOTE.—The relative fractions of each class are listed.

[5] Spectral type obtained from the template fitting in the photometric redshift technique (Dahlen et al. 2005).

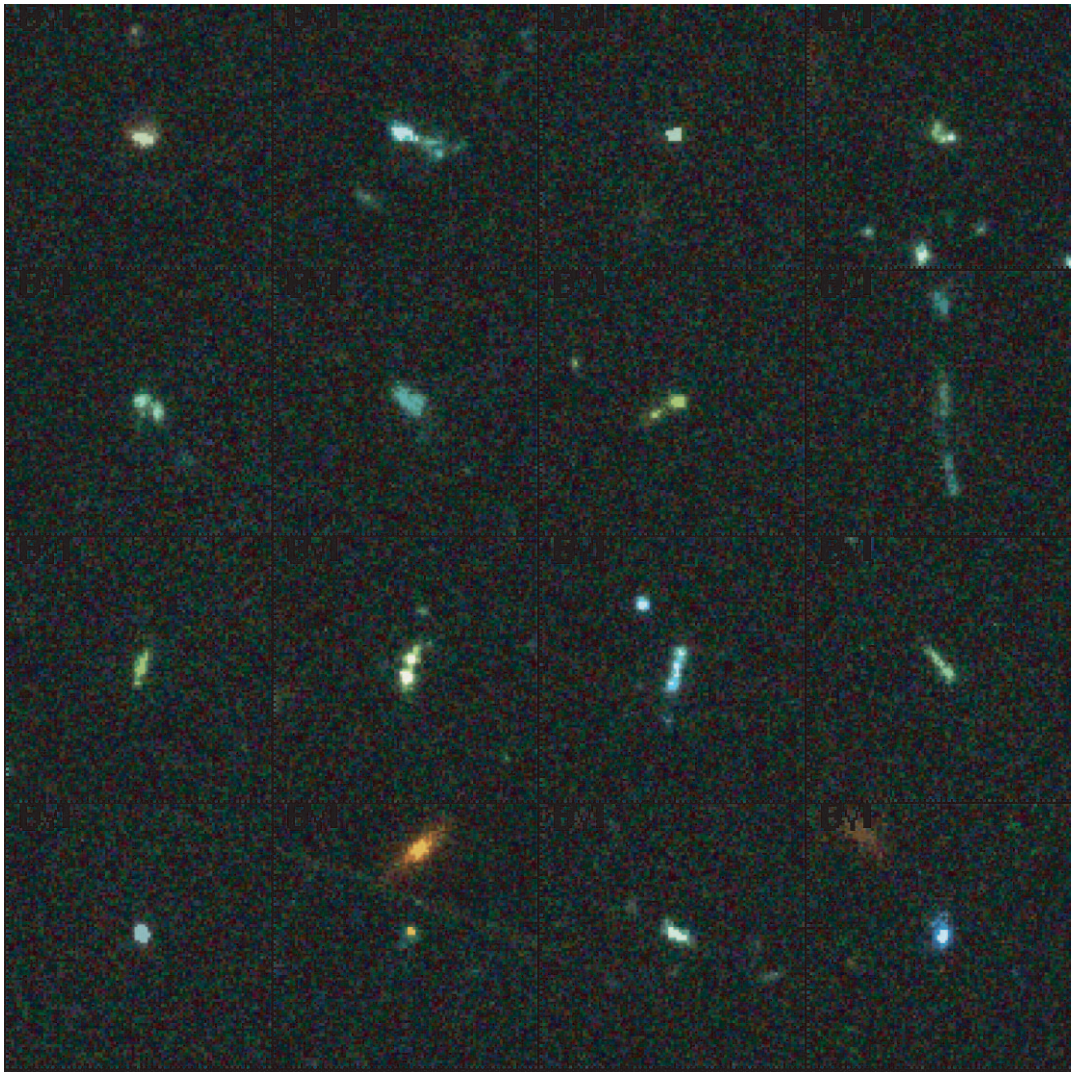

FIG. 6.—*BVi* color composite of 16 bright *U*-band dropouts in our sample. Each cutout is $5'' \times 5''$ in size. The dropout galaxy is located at the center of each panel.

and clump+doubles+tadpoles), indicating that about 50% of the star formation takes place in clumps over an extended redshift range of $0.8 \lesssim z \lesssim 3.5$.

5. DROPOUT STATISTICS

It is interesting to compare the statistical properties of the dropouts selected here with those in the two HDFs. The selection procedures are very similar, although slight differences can arise from the different filter sets available and from the different depths of the observations; those used here are significantly deeper in *U* but shallower in the other bands. With those caveats in mind, we compute some properties of interest for our sample.

5.1. *Number Density*

We have identified 125 *U*-band dropouts in the 5.67 arcmin^2 of sky over which we have multiwavelength data available. Of these, 80 fall within the full-depth coverage of our F300W data, which cover 4.02 arcmin^2. The surface density of dropouts at the full depth of our study is thus 19.9 sources arcmin^{-2}, similar within the statistical uncertainties to the 17.5 sources arcmin^{-2} found in the HDF-S data (C00). Relative to the HDF-N value of 16.0 sources arcmin^{-2} our measured surface density is higher with a marginal significance. Both the HDF measurements were obtained using the Madau et al. (1996) color selection criteria and only included sources brighter than $B_{450} = 26.79$. Our sample uses a different filter combination with its own color selection criterion and all sources brighter than $B = 27.3$.

Using only the dropouts in the region with full depth and assuming that these dropouts uniformly probe the redshift range $2 \lesssim z \lesssim 3.5$, we obtain a comoving galaxy density of 4.0×10^{-3} Mpc^{-3} for the concordance cosmology we adopt, corresponding to 5.7×10^{-3} Mpc^{-3} with the cosmology adopted by Madau et al. (1996; $q_0 = 0.5$, $h_{100} = 0.5$, and no cosmological constant). For comparison, they report a density of 4.2×10^{-3} Mpc^{-3} from the HDF-N. Our somewhat higher galaxy density may be due in part to the increased depth of our sample, although cosmic variance can also play an important role in such small areas.

5.2. *Star Formation Rate Density Evolution*

A key measure is the evolution of the cosmic SFR density as a function of lookback time (or redshift) (e.g., Madau et al. 1996). The SFR can be measured using carefully calibrated proxies such as the luminosity in the X-ray (Ranalli et al. 2003), radio (Condon et al. 1992), far-IR (Kennicutt 1998), narrowband line emission (Moustakas et al. 2006), and the rest-frame UV continuum (Madau et al. 1998). When such indicators are used to compute

the SFR for the *same* sample, they are consistent to within a factor of 2 (Daddi et al. 2004).

Even within various samples identified using the dropout technique, significant discrepancies may exist. These may be caused by cosmic variance, differences in stellar population synthesis models, or in the treatment of dust attenuation. Different assumptions about the shape of the luminosity function and the differing photometric uncertainties in observations of different depths can also introduce systematics into the measurement. Of these, the uncertainties in the dust obscuration correction are of the greatest concern in estimating the SFR from the rest-frame UV continuum. Recently, Heckman et al. (2005) have obtained *Galaxy Evolution Explorer* observations of compact UV-luminous galaxies in the local universe. They find that these galaxies, which are chosen to have rest-frame UV luminosities similar to those of $z \sim 3$ star-forming galaxies, also match them in stellar mass, velocity dispersions, and gas-phase metallicity. Like their distant counterparts, these galaxies are forming stars at a rate high enough to build their present-day stellar mass in 1–2 Gyr. For these local galaxies, dust attenuation is relatively modest: 0.5–2 mag. If the high-redshift galaxies exhibit similar dust properties, the effect of uncertainty in dust attenuation on the computed star formation rate may be less than previously thought (Vijh et al. 2003).

In spite of these uncertainties, general trends in the evolution of the SFR density as computed from the UV continuum luminosity have become apparent over the last decade. We now know with a high level of confidence that the SFR density steadily increases from the local universe out to a redshift of $z \sim 3$ and then either shows a falloff or remains steady at higher redshifts (e.g., Lilly et al. 1996; Madau et al. 1996; Dickinson 1998; Steidel et al. 2003; Bouwens et al. 2004). We adopt here the formulation of C00, which in turn follows the prescriptions of Steidel et al. (1999). For ease of comparison with Figure 11 of C00 we use their cosmological parameters $(h, \Omega_m, \Omega_\Lambda, \Omega_{\rm tot}) = (0.65, 0.3, 0.7, 1)$ and define a fiducial magnitude $R_{606+775}$ for each candidate, which is the average of the *V* and *i* magnitudes. We use this magnitude to compute $m_{\rm AB,tot}$, which is the total integrated flux of the Lyman break candidates. To avoid variable levels of incompleteness, we only use dropouts in the full-depth region of our image for computing the integrated flux. Then, the star formation rate density at a mean redshift z between two redshifts z_1, z_2 is given by

$$\log\left(\frac{\rm SFR}{M_\odot\ {\rm yr}^{-1}\ {\rm Mpc}^{-3}}\right) = 2\log\frac{D_L(z)}{\rm cm} - 0.4m_{\rm AB,tot} - \log\frac{\Delta V(z_1,z_2)}{\rm Mpc^3} - \log A + \log\delta L - \log(1+z) - 34.516, \quad (3)$$

where the redshifts z, z_1, and z_2 are 2.75, 2.00, and 3.50, respectively, D_L is the luminosity distance, ΔV is the total volume between the two redshifts, and A is the area of the field of view in square arcseconds. The contribution of galaxies fainter than our detection threshold is included via the correction factor δL, which is obtained by integrating the assumed luminosity function (Steidel et al. 1999) from our survey limit down to $0.1L^*$ (eq. [9], C00). The above formula includes a uniform extinction correction factor of 4.7 (Steidel et al. 1999) to the measured UV luminosity densities. This correction factor is appropriate for a typical extinction $E(B-V) = 0.15$ and the Calzetti (1997) reddening law.

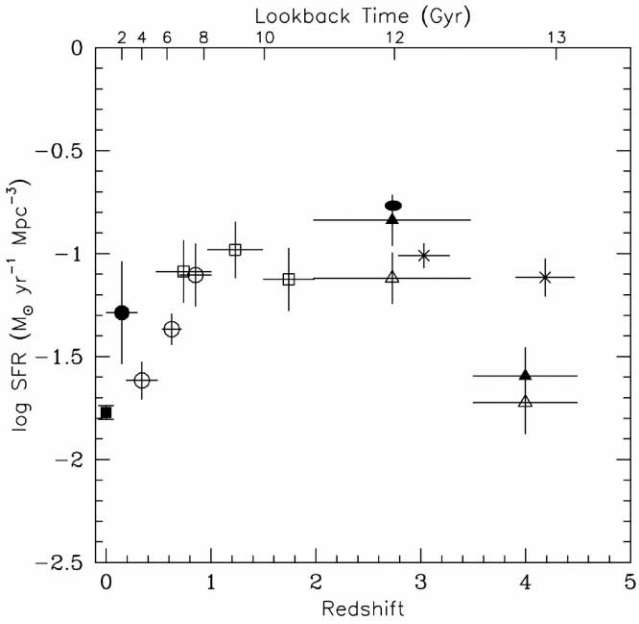

FIG. 7.—SFR density evolution as a function of redshift (compare to Fig. 11 of C00). The SFR is estimated from the UV luminosity density. The $z > 2$ points are from Lyman break objects in the HDF-N (*open triangles*), in the HDF-S from C00 (*filled triangles*), and in the Steidel et al. (1999) ground-based survey (*crosses*). The black ellipse indicates the SFR density measured in this work. For clarity, error bars are not plotted for our data point. Errors along the redshift axis are identical to the HDF points. The statistical error on the SFR density axis is about 0.09. Distances and volumes are computed using the cosmological parameters $(h, \Omega_m, \Omega_\Lambda, \Omega_{\rm tot}) = (0.65, 0.3, 0.7, 1.0)$. At lower redshifts, only results that are directly comparable to the high-redshift data are plotted. The open squares are from HDF photometric redshifts by Connolly et al. (1997), the open circles are from Lilly et al. (1996), the filled square is from the Hα survey of Gallego et al. (1995), and the filled circle is from Sullivan et al. (2000).

We measure an integrated SFR density of $0.18\,M_\odot\,{\rm yr}^{-1}\,{\rm Mpc}^{-3}$. This value is only marginally higher than that measured for the HDF-S, which in turn is higher than that measured for the HDF-N. Both these values were measured by the authors of C00, using identical source detection and photometry procedures with data of similar depth obtained using the same set of filters and with the same color selection criteria. We show in Figure 7 the evolution of SFR density with redshift, comparing our measurement with other measurements from the literature obtained using a similar technique.

Measurements of the statistical properties of any clustered population are plagued by uncertainty due to cosmic variance, the field-to-field variation due to large-scale structure (Somerville et al. 2004). At high redshifts, especially with the small few-arcminute-sized field of view of *HST*, the volume sampled for $2.0 \lesssim z \lesssim 3.5$ is $\sim 10^4\,{\rm Mpc}^3$, small enough that cosmic variance is a significant source of uncertainty. The variance of number counts N over an area A on the sky in the presence of a nonzero angular autocorrelation function is given by (Peebles 1980)

$$\sigma^2(N) = nA + n^2\int_{A_1} dA_1 \int_{A_2} dA_2\, w(\theta), \quad (4)$$

where n is the average density of objects, and thus nA is the expectation value of N, and $w(\theta)$ is the two-point angular autocorrelation function between points A_1 and A_2. For our full-depth area of 4.02 arcmin^2, the second term in equation (4) can be approximated as $1.8n^2A^2A_w$, where A_w is the two-point angular correlation of the sample at a scale of $1'$. This assumes that the angular correlation function obeys a power law with exponent

$\beta = -1.2$ as measured by Giavalisco & Dickinson (2001) for a combined sample of U dropouts from the two HDFs. We estimate the value of A_w to be 0.02 at $1'$ from the 1 σ upper limit on their measured angular correlation function for their combined HDF sample. The total expected variance is thus:

$$\sigma^2(N) = 80 + 1.8 \times 0.02 \times 80^2 = 310.4, \qquad (5)$$

or approximately 3.9 times larger than the Poisson contribution alone. The expected rms fluctuation in number counts is about 17.6 galaxies over the full-depth area compared with 8.9 for the Poisson case. This corresponds to an uncertainty of 0.09 in the logarithm of the SFR density, and can be treated as the nominal statistical uncertainty for our measurement. It should be noted that this error bar only accounts for statistical uncertainties; systematic offsets, e.g., due to incorrect dust corrections, may be significantly larger.

An effective way to reduce the uncertainty caused by clustered populations is to obtain samples of high-redshift galaxies along independent lines of sight. Our measurement of the SFR density in the GOODS-S area provides such an independent measurement and is in fact only the third such measurement obtained exclusively from space-based data at $z \sim 3$. Within the error bars our measurement of SFR density is consistent with the value measured for HDF-S, indicating that the range of variation in SFR density is probably well sampled by the two HDFs.

In the future, the second WFPC2 F300W parallels, if combined with additional new data in the BV filters, can provide a fourth space-based measurement of the SFR density at $z \sim 3$, further reducing the impact of cosmic variance.

We thank the GOODS and HUDF teams for the magnificent public data that made this work possible. We are grateful to the referee, G. Zamorani, for insightful comments and suggestions that helped improve the content and presentation of this paper. We thank Harry Ferguson and Uma Vijh for fruitful discussions on different aspects of this paper. Support for program AR 9540 was provided by NASA through a grant from the Space Telescope Science Institute, which is operated by the Association of Universities for Research in Astronomy, Inc., under NASA contract NAS5-26555.

REFERENCES

Abraham, R. G., Tanvir, N. R., Santiago, B. X., Ellis, R. S., Glazebrook, K., & van den Bergh, S. 1996, MNRAS, 279, L47
Beckwith, S. V. W., et al. 2006, AJ, submitted
Bertin, E., & Arnouts, S. 1996, A&AS, 117, 393
Bouwens, R. J., et al. 2004, ApJ, 606, L25
Bruzual, G., & Charlot, S. 2003, MNRAS, 344, 1000 (BC03)
Calzetti, D. 1997, AJ, 113, 162
Casertano, S., & Wiggs, M. S. 2001, An Improved Geometric Solution for WFPC2 (WFPC2 Instrum. Sci. Rep. 2001-10; Baltimore: STScI)
Casertano, S., et al. 2000, AJ, 120, 2747 (C00)
Chabrier, G. 2003, PASP, 115, 763
Charlot, S., & Fall, S. M. 2000, ApJ, 539, 718
Condon, J. J. 1992, ARA&A, 30, 575
Connolly, A. J., Szalay, A. S., Dickinson, M., SubbaRao, M. U., & Brunner, R. J. 1997, ApJ, 486, L11
Daddi, E., Cimatti, A., Renzini, A., Fontana, A., Mignoli, M., Pozzetti, L., Tozzi, P., & Zamorani, G. 2004, ApJ, 617, 746
Dahlen, T., Mobasher, B., Somerville, R. S., Moustakas, L. A., Dickinson, M., Ferguson, H. C., & Giavalisco, M. 2005, ApJ, 631, 126
de Mello, D. F., Wadadekar, Y., Dahlen, T., Casertano, S., & Gardner, J. P. 2006, AJ, 131, 216
Dickinson, M. 1998, in The Hubble Deep Field, ed. M. Livio, S. M. Fall, & P. Madau (New York: Cambridge Univ. Press), 219
Elmegreen, B. G., & Elmegreen, D. M. 2005, ApJ, 627, 632
Elmegreen, D., Elmegreen, B., Rubin, D., & Schaffer, M. 2005, ApJ, 631, 85
Fruchter, A. S., & Hook, R. N. 2002, PASP, 114, 144
Gallego, J., Zamorano, J., Aragon-Salamanca, A., & Rego, M. 1995, ApJ, 455, L1
Giavalisco, M. 2002, ARA&A, 40, 579
Giavalisco, M., & Dickinson, M. 2001, ApJ, 550, 177
Giavalisco, M., et al. 2004, ApJ, 600, L93
Heckman, T. M., et al. 2005, ApJ, 619, L35
Heyer, I., et al. 2004, WFPC2 Instrument Handbook, ver. 9.0 (Baltimore: STScI)
Kennicutt, R. C., Jr. 1998, ARA&A, 36, 189
Kozhurina-Platais, V., Anderson, J., & Koekemoer, A. M. 2003, Toward a Multi-Wavelength Geometric Distortion Solution for WFPC2 (WFPC2 Instrum. Sci. Rep. 2003-02; Baltimore: STScI)
Le Borgne, J.-F., et al. 2003, A&A, 402, 433
Le Fèvre, O., et al. 2005, Nature, 437, 519
Lilly, S. J., Le Févre, O., Hammer, F., & Crampton, D. 1996, ApJ, 460, L1
Madau, P. 1995, ApJ, 441, 18
Madau, P., Ferguson, H. C., Dickinson, M. E., Giavalisco, M., Steidel, C. C., & Fruchter, A. 1996, MNRAS, 283, 1388
Madau, P., Pozzetti, L., & Dickinson, M. 1998, ApJ, 498, 106
Meiksin, A. 2006, MNRAS, 365, 807
Moustakas, J., Kennicutt, R. C., Jr., & Tremonti, C. A. 2006, ApJ, 642, 775
Oke, J. B., & Gunn, J. E. 1983, ApJ, 266, 713
Papovich, C., et al. 2005, ApJ, 631, 101
Peebles, P. J. E. 1980, The Large Scale Structure of the Universe (Princeton: Princeton Univ. Press)
Ranalli, P., Comastri, A., & Setti, G. 2003, A&A, 399, 39
Reddy, N. A., Erb, D. K., Steidel, C. C., Shapley, A. E., Adelberger, K. L., & Pettini, M. 2005, ApJ, 633, 748
Rix, H.-W., et al. 2004, ApJS, 152, 163
Salpeter, E. E. 1955, ApJ, 121, 161
Somerville, R. S., Lee, K., Ferguson, H. C., Gardner, J. P., Moustakas, L. A., & Giavalisco, M. 2004, ApJ, 600, L171
Steidel, C. C., Adelberger, K. L., Giavalisco, M., Dickinson, M., & Pettini, M. 1999, ApJ, 519, 1
Steidel, C. C., Adelberger, K. L., Shapley, A. E., Pettini, M., Dickinson, M., & Giavalisco, M. 2003, ApJ, 592, 728
Sullivan, M., Treyer, M. A., Ellis, R. S., Bridges, T. J., Milliard, B., & Donas, J. 2000, MNRAS, 312, 442
Tinsley, B. M. 1980, Fundam. Cosm. Phys., 5, 287
van den Bergh, S. 2002, PASP, 114, 797
Vijh, U. P., Witt, A. N., & Gordon, K. D. 2003, ApJ, 587, 533
Wadadekar, Y., et al. 2006, PASP, 118, 450
Williams, R. E., et al. 1996, AJ, 112, 1335
Windhorst, R., et al. 2002, ApJS, 143, 113